LETTERS
https://doi.org/10.1038/s41566-022-01010-1

nature photonics

Check for updates

OPEN

Observation of light-driven band structure via multiband high-harmonic spectroscopy

Ayelet J. Uzan-Narovlansky[1,2], Álvaro Jiménez-Galán[3,4], Gal Orenstein[5], Rui E. F. Silva[6], Talya Arusi-Parpar[1], Sergei Shames[1], Barry D. Bruner[1], Binghai Yan[7], Olga Smirnova[3,8], Misha Ivanov[3,9,10] and Nirit Dudovich[1]✉

Intense light–matter interactions have revolutionized our ability to probe and manipulate quantum systems at sub-femtosecond timescales[1], opening routes to the all-optical control of electronic currents in solids at petahertz rates[2–7]. Such control typically requires electric-field amplitudes in the range of almost volts per angstrom, when the voltage drop across a lattice site becomes comparable to the characteristic bandgap energies. In this regime, intense light–matter interaction induces notable modifications to the electronic and optical properties[8–10], dramatically modifying the crystal band structure. Yet, identifying and characterizing such modifications remain an outstanding problem. As the oscillating electric field changes within the driving field's cycle, does the band structure follow and how can it be defined? Here we address this fundamental question, proposing all-optical spectroscopy to probe the laser-induced closing of the bandgap between adjacent conduction bands. Our work reveals the link between nonlinear light–matter interactions in strongly driven crystals and the sub-cycle modifications in their effective band structure.

The ability of near-resonant light fields to modify the energetics and dynamics of an atom (or a molecule) is central to many phenomena such as laser cooling, trapping, quantum optics of atoms in a cavity[11,12] or extremely efficient generation of hyper-Raman lines[13]. The combined states of matter and near-resonant light are generally studied over many laser cycles using the Floquet formalism, which takes advantage of the periodicity of light oscillations. In solids, cycle-averaged modification of the hopping rates between the neighbouring sites leads to, for example, the coherent destruction of tunnelling[14] and modified local interaction potentials[10].

The situation changes in light fields with frequencies well below resonance but with intensities sufficiently high to induce electronvolt-scale voltages across a lattice site. As the oscillating electric field of the lightwave changes from zero to its maximum value within a quarter cycle, rapidly changing voltages can lead to sub-cycle modifications of the macroscopic properties, such as transmittance[4,6] or conductance[7]. In this regime, a cycle-averaged frequency-domain Floquet perspective is hardly satisfying.

Here we describe how the effective band structure can be introduced in such an interaction regime within a time-domain perspective. We experimentally demonstrate all-optical spectroscopy of a strongly driven crystal, revealing an anomalous spectral intensity response, using high-harmonic generation (HHG). Our theoretical study links these observations to laser-induced closing of the gap between adjacent conduction bands (Fig. 1a).

HHG in solids involves optical tunnelling[15] across the gap between the valence and conduction bands. This transition initiates harmonic generation associated with both intraband currents[10,16,17] and electron–hole recombination, the latter leading to higher-order harmonic emission[18]. At higher light intensities and/or lower frequencies, one enters a new dynamical regime. In many systems, as the electron–hole wavepacket approaches the edges of the Brillouin zone, Landau–Dykhne-type transitions[19] can promote electrons to higher conduction bands, as reflected in the harmonic spectra[20,21] (Fig. 1a). However, can the imprint of these transitions on high-harmonic emission be used to observe light-induced modifications of the bands?

One can show that light-induced modifications of the bands are directly linked to the sub-cycle Landau–Dykhne-type transitions between them (Methods). In the low-frequency limit, one begins with the adiabatic approximation, which treats the phase ωt of the electric-field oscillations as a parameter, and finds the adiabatic band structure $\epsilon(k,\omega t)$ in the presence of a quasi-static electric field. When a non-adiabatic Landau–Dykhne-type transition between a pair of bands occurs, typically as the electron is laser driven across the minimal bandgap, it modifies the gap as follows:

$$\Delta\epsilon_{\mathrm{eff}}(t) \simeq \Delta\epsilon_{\mathrm{ad}}(t)\sqrt{\frac{1-w_{\mathrm{LD}}(t)}{1+w_{\mathrm{LD}}(t)}}, \qquad (1)$$

where $\Delta\epsilon_{\mathrm{eff}}$ is the effective bandgap, $\Delta\epsilon_{\mathrm{ad}}$ is the bandgap in the adiabatic approximation and w_{LD} is the probability of the sub-cycle Landau–Dykhne-type transition. The result is intuitive: the effective bandgap is closed by the laser field when the sub-cycle transition approaches unity, that is, $w_{\mathrm{LD}}(t)\simeq 1$. Given the exponential sensitivity of $w_{\mathrm{LD}}(t)$ to the laser-field strength, the effective bandgap closes soon after the sub-cycle excitation probability becomes appreciable.

To experimentally investigate this phenomenon, we use two-colour HHG spectroscopy[22,23] (Fig. 1b), augmenting the strong fundamental driver with a weak second-harmonic (SH) field and controlling their sub-cycle delay τ. Electron–hole trajectories

[1]Department of Complex Systems, Weizmann Institute of Science, Rehovot, Israel. [2]Department of Physics, Princeton University, Princeton, NJ, USA. [3]Max-Born-Institut, Berlin, Germany. [4]Joint Attosecond Science Laboratory, National Research Council of Canada and University of Ottawa, Ottawa, Ontario, Canada. [5]SLAC National Accelerator Laboratory, Stanford University, Stanford, CA, USA. [6]Instituto de Ciencia de Materiales de Madrid (ICMM), Consejo Superior de Investigaciones Científicas (CSIC), Madrid, Spain. [7]Department of Condensed Matter, Weizmann Institute of Science, Rehovot, Israel. [8]Technische Universität Berlin, Ernst-Ruska-Gebäude, Berlin, Germany. [9]Blackett Laboratory, Imperial College London, London, UK. [10]Department of Physics, Humboldt University, Berlin, Germany. ✉e-mail: nirit.dudovich@weizmann.ac.il

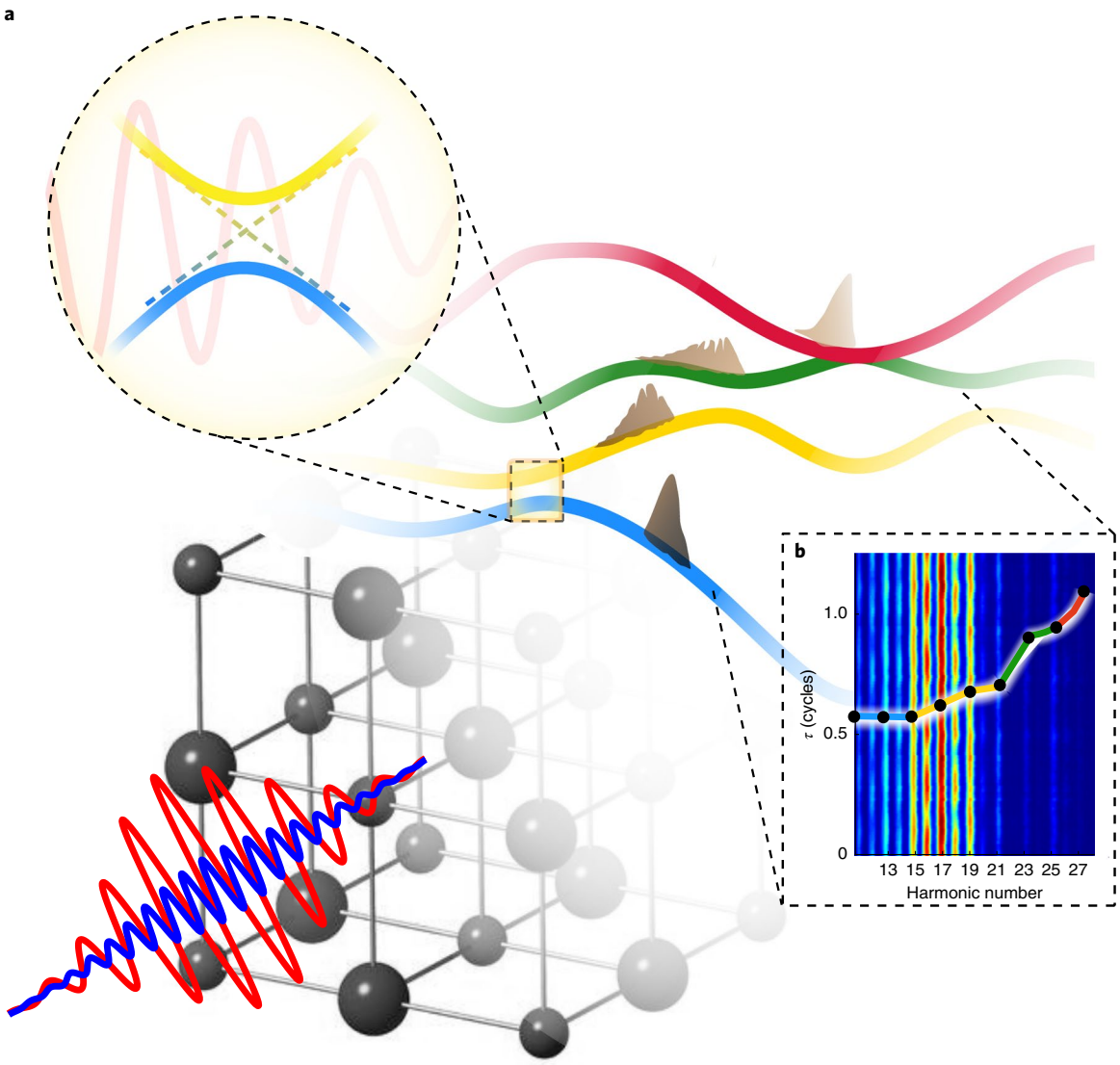

Fig. 1 | All-optical spectroscopy of dynamical band structure. a, Non-adiabatic Landau–Dykhne-type transition between a pair of bands. **b**, Two-colour HHG spectroscopy probes the internal dynamics, mapping the temporal properties of electron trajectories, transitions between the bands as well as their laser-driven modifications.

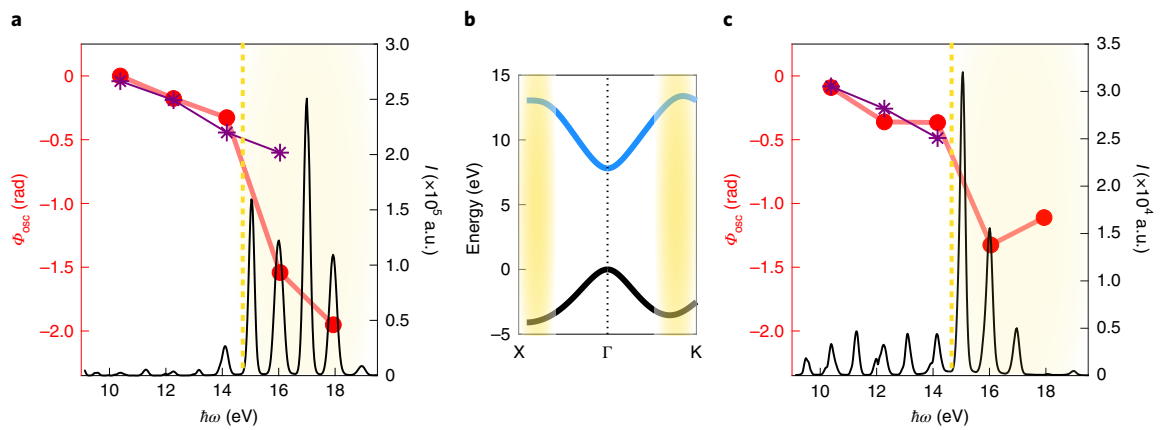

Fig. 2 | HHG spectroscopy beyond the semi-classical description. a,**c**, HHG spectrum (black line) and oscillation phase (red dots) as a function of photon energy for crystal orientations of 0° (**a**) and 45° (**c**). The oscillation phase calculated using the saddle-point approximation in the interband model[18] (purple star markers). **b**, Valence and the first conduction band for 0° (Γ to X) and for 45° (Γ to K). The yellow-shaded area emphasizes the energy range where the semi-classical description fails[21], also marked at the corresponding photon energies in **a** and **c** (dashed yellow line).

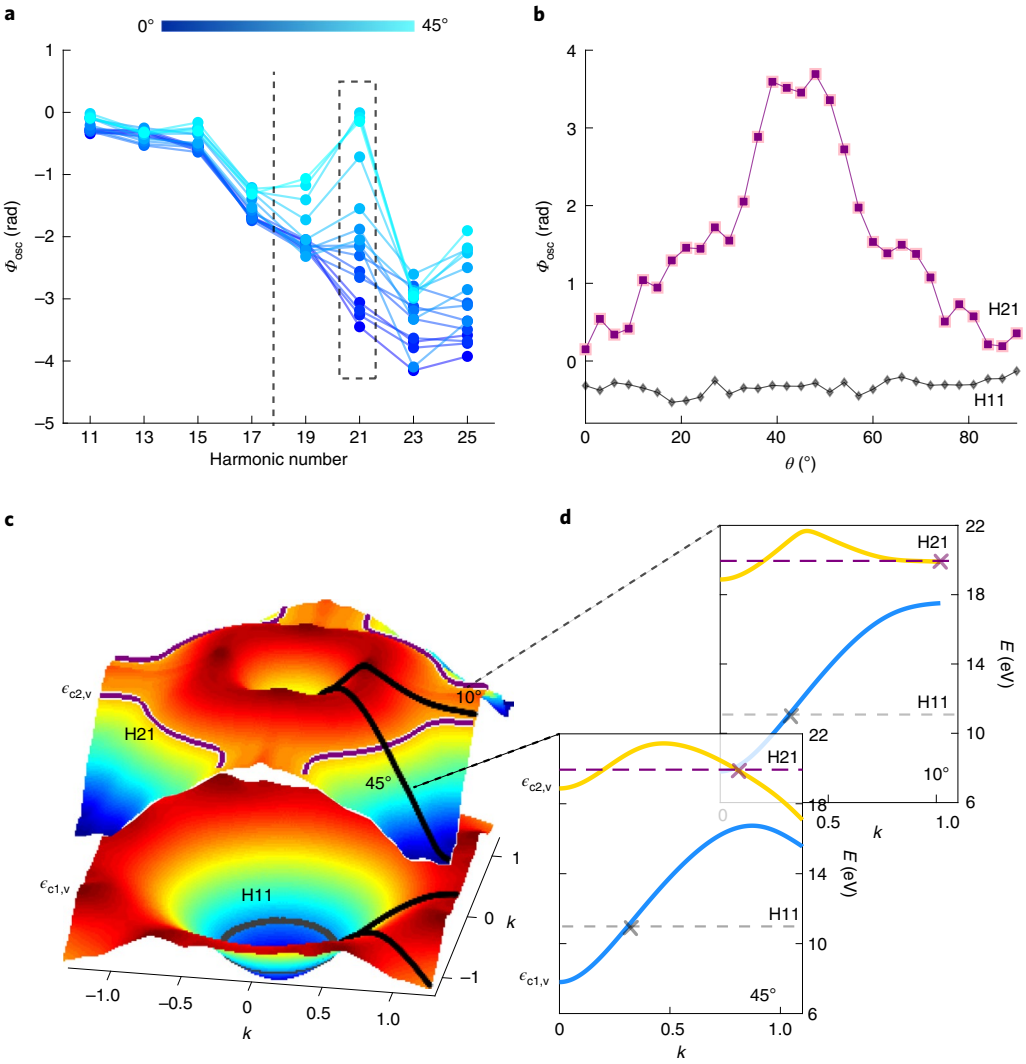

Fig. 3 | Probing the structural dependence of multiple conduction bands. a, Oscillation phase as a function of harmonic number, for different crystal orientations ranging from 0° (dark blue) to 45° (cyan). The dashed line marks the cutoff of the first conduction band and the dashed box emphasizes the H21 oscillation phases for different orientations (plotted in **b**). **b**, Harmonic 21 (H21, purple) and harmonic 11 (H11, grey) oscillation phase as a function of crystal orientation. **c**, Two-dimensional second bandgap, $\epsilon_{c2,v}=\epsilon_{c2}-\epsilon_{v}$, as a function of crystal momentum (top). The purple contour represents the H21 energy along different crystal orientations. Two-dimensional first bandgap, $\epsilon_{c1,v}=\epsilon_{c1,v}-\epsilon_{v}$, as a function of crystal momentum (bottom). The grey contour represents H11 energy along different crystal orientations. **d**, One-dimensional cut of the second (yellow) and first (blue) bandgap along crystal orientations of 10° and 45°. H21 and H11 energies are represented by the purple and grey dashed lines, as well as their crossing point with the bandgaps (cross markers).

responsible for different harmonics[24] are perturbed by the weak field: each trajectory acquires an additional complex phase $\sigma(\tau)$, which is accumulated along the entire trajectory, serving as a sensitive label of its temporal properties. If the fundamental field generates only odd harmonics, the SH field breaks the symmetry of interaction, as $\sigma(\tau)$ changes sign between two consecutive half-cycles (Supplementary Information). This phase is mapped into the harmonic intensity as

$$I_{\mathrm{odd}}(\sigma(\tau)) \propto (\mathrm{e}^{\mathrm{i}\sigma} + \mathrm{e}^{-\mathrm{i}\sigma}),$$
$$I_{\mathrm{even}}(\sigma(\tau)) \propto (\mathrm{e}^{\mathrm{i}\sigma} - \mathrm{e}^{-\mathrm{i}\sigma}). \quad (2)$$

Scanning τ modifies $\sigma(\tau)$ in a periodic manner, modulating the harmonic spectrum. The modulation phase and contrast encode the dynamical properties of electron trajectories associated with each harmonic order and allow their reconstruction with attosecond precision. In previous studies this method resolved the interband contribution to high-harmonic emission[24] and provided an all-optical reconstruction of the field-free band structure on exciting a single conduction band[25,26]. In this paper, we use this scheme to study the underlying dynamics of driven multiband currents, probing the dressed band structure.

Experiments were performed on MgO (ref. [27]) using $\lambda = 1.3\,\mu\mathrm{m}$ laser field at intensities of $\sim 10^{13}\,\mathrm{W\,cm^{-2}}$ and a weak SH field, polarized parallel to the fundamental field. We have measured the HHG modulations with the two-colour delay and extracted the oscillation phase Φ_N associated with each harmonic order N. Figure 2 presents Φ_N as a function of the harmonic order for orientation angles of 0° (ΓX) and 45° (ΓK) with respect to the fundamental field's polarization. For harmonics $N = 11-15$ (10.5–14.5 eV), which are associated with electron–hole recombination from the first conduction band, we measure a gradual slope of Φ_N with N. The slope reflects the evolution of the trajectory length with harmonic order[24], supported by our semi-classical calculations (Supplementary Information).

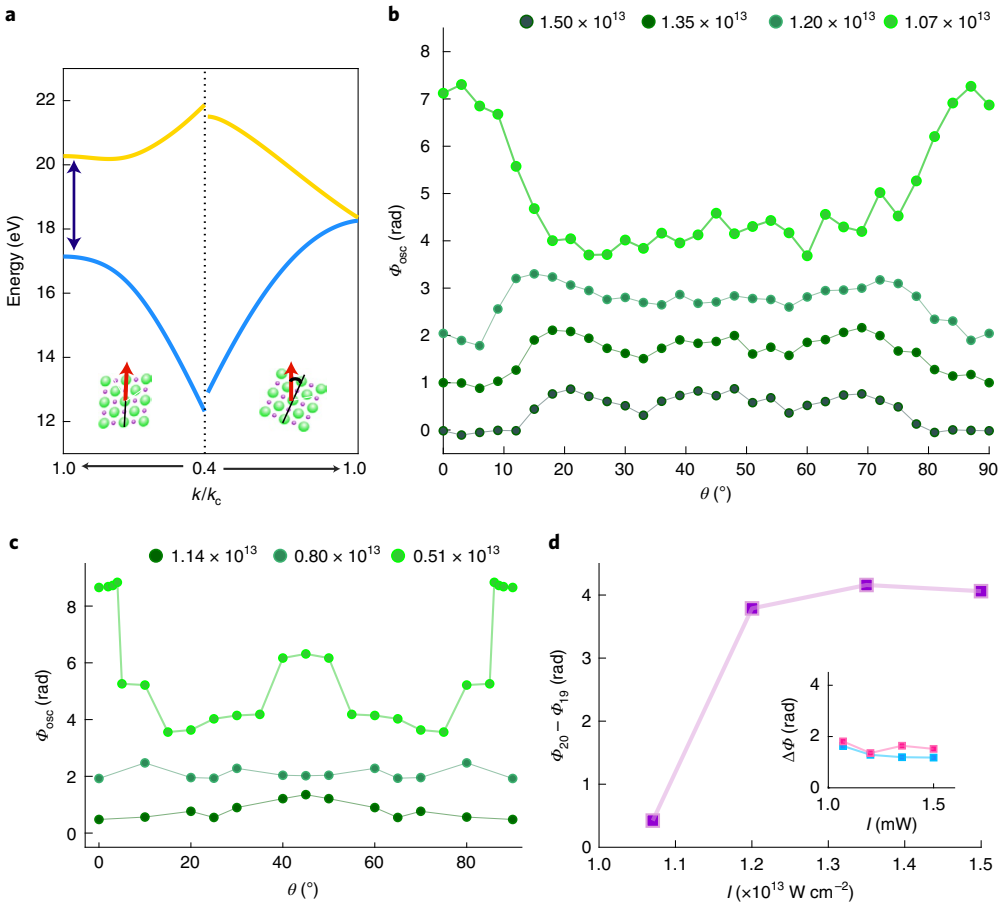

Fig. 4 | Dynamical band structure. a, First (blue) and second (yellow) bandgaps, $\epsilon_{c1,v}$ and $\epsilon_{c2,v}$, respectively, for 0° (right) and 25° (left) orientations, as a function of k/k_c ($k_c = 2\pi/a$, where a is the lattice constant). **b**, H20 oscillation phase as a function of crystal orientation for different fundamental field intensities (light green to dark green). **c**, Calculated oscillation phase of H20 as a function of crystal orientation for different fundamental field intensities (light green to dark green). **d**, Oscillation phase difference, $\Phi_{20} - \Phi_{19}$, at 0° orientation as a function of the fundamental field intensities. The inset shows the $\Phi_{18} - \Phi_{17}$ (pink) and $\Phi_{22} - \Phi_{21}$ (blue) plots.

As we approach the edge of the Brillouin zone, represented by harmonic 17 (H17; 16 eV) for the ΓK direction and harmonic 19 (H19) for the Γ–X direction, this simple description fails. A clear phase jump appears in the measurements, associated with the edge of the zone and changing the band curvature. At this point, the mapping between momentum and energy becomes singular, leading to the appearance of spectral caustic[21]. Thus, the phase measurement serves as a sensitive probe of the bandgap and allows its accurate identification.

Beyond the cutoff energy of the first conduction band, the electron dynamics involve multiple bands[20,28]. The harmonic emission is dictated by electron currents originating from higher conduction bands, determined by their structure and coupling. Importantly, these parameters depend on the crystal orientation, with each orientation offering a new one-dimensional slice of the band structure[27,29]. We can, thus, track the dependence of electron dynamics on the band structure and laser-induced couplings by resolving the oscillation phase of each harmonic as a function of crystal orientation.

Figure 3a presents the HHG oscillation phase, for various crystal orientations. The oscillation phases of the lower harmonics (H11, H13 and H15) emitted far from the edge of the Brillouin zone remain unchanged with the crystal orientation. Indeed, the bottom of the first conduction band, as well as its distance from the valence band ($\epsilon_{c1,v} = \epsilon_{c1} - \epsilon_v$), is approximately isotropic (Fig. 3c).

For higher harmonics ($N = 19$–29), a strong variation in the oscillation phase with crystal orientation is observed (Fig. 3a). Figure 3b presents the oscillation phase as a function of crystal orientation for H21. The phase shows a sharp increase by more than π as the orientation angle changes towards 45°. The origin of this sharp variation can be understood by looking at the angular dependence of the bands. Figure 3c shows the energy difference between the valence, first and second conduction bands ($\epsilon_{c1,v}$, $\epsilon_{c2,v}$) for different crystal orientations, together with the energy contours for H21. The crystal momentum at the emission point associated with H21 quickly changes with the crystal orientation (Fig. 3d). The strong orientation-dependent modifications of the bandgap, $\epsilon_{c2,v}$, lead to notable angular changes of the corresponding electron trajectories, as captured by the phase measurement. In contrast, the emission points for H11–H15 are almost constant with the crystal orientation (Fig. 3d). Such nearly isotropic response is captured by the phase measurement, too (Fig. 3b).

We now turn to resolving the light-induced dressing of the band structure. Although in large bandgap materials, such as MgO, observing the bandgap modifications requires high intensities, and the gap between the conduction bands is relatively small. Therefore, it can be notably modified at moderate field intensities. We focus on harmonic emission associated with an energy gap between the first and second conduction bands. In Fig. 4a, we plot the field-free band structure, which provides a good description of the system at

low laser intensities. At 0° orientation, the minimum energy gap between the two conduction bands, $\epsilon_{c2}-\epsilon_{c1}$, is around 3 eV; H20 is located inside this gap. As we rotate the crystal, the energy gap rapidly reduces to zero, and H20 is emitted from the second conduction band. In Fig. 4b, we plot the oscillation phase of H20 (Φ_{20}) as a function of crystal orientation for different laser intensities. At low intensity (light green), Φ_{20} shows a dramatic angular dependence, mainly between 0° and 25° as a consequence of the strong angular dependence of $\epsilon_{c2}-\epsilon_{c1}$. Importantly, as we increase the field intensity, the angular dependence of Φ_{20} decreases and then notably flattens (dark green). These experimental results are confirmed by our numerical simulations (Fig. 4c). Numerically, the flattening of the angular dependence of the oscillation phase coincides with the onset of strong sub-cycle Landau–Dykhne-type transitions, with the probability approaching 50% (Supplementary Information).

Our theoretical and numerical results link these intensity-dependent observations with the closing of the effective bandgap by the laser field. According to equation (2), the oscillation phase is dictated by the additional complex phase σ induced by the SH field[23]. The imaginary component, Im(σ), is associated with perturbations of tunnelling and recombination probabilities, whereas the real component Re(σ) reflects subtle modifications in the electron trajectory as it propagates within the band. Since the odd and even harmonics represent constructive and destructive interference of two sub-cycle emissions, Re(σ) leads to an oscillation phase difference. However, Im(σ) simultaneously affects both even and odd harmonics; therefore, their oscillation phases coincide (Supplementary Information).

In Fig. 4d, we plot the relative oscillation phase of H19 and H20, namely, $\Phi_{20}-\Phi_{19}$, at 0° orientation for different fundamental field intensities. At a sufficiently low laser intensity, this phase difference vanishes, reflecting the dominant role of the imaginary component. The origin of this imaginary component could be associated with an anomalous emission event of these harmonics, emitted from an energy gap. At higher field intensities, the band structure is strongly dressed so that the energy gap between the bands becomes negligible. Therefore, the associated imaginary component is reduced and the perturbation is dominated by Re(σ), leading to a phase difference between the even and odd harmonics (Supplementary Information).

In summary, our study establishes the all-optical spectroscopy of a strongly driven crystal, revealing a laser-induced modification of the band structure. We identify the dynamical transitions between several conduction bands as well as probe their structural dependence. Importantly, we resolve the clear signature of harmonic emission from the energy gap between the two conduction bands, probing its modification by the laser field. This study provides a general framework for resolving and interpreting attosecond electronic response phenomena in strongly driven solids. Looking forward, two-colour HHG spectroscopy opens a window into the observation of a broad range of electronic phenomena—from sub-cycle phase transitions to ultrafast dynamics in correlated systems; some of these have been theoretically predicted decades ago, whereas others are still hotly debated.

Online content

Any methods, additional references, Nature Research reporting summaries, source data, extended data, supplementary information, acknowledgements, peer review information; details of author contributions and competing interests; and statements of data and code availability are available at https://doi.org/10.1038/s41566-022-01010-1.

Received: 11 August 2021; Accepted: 21 April 2022;
Published online: 2 June 2022

References

1. Corkum, P. á & Krausz, F. Attosecond science. *Nat. Phys.* **3**, 381–387 (2007).
2. Garg, M. et al. Multi-petahertz electronic metrology. *Nature* **538**, 359–363 (2016).
3. Langer, F. et al. Lightwave valleytronics in a monolayer of tungsten diselenide. *Nature* **557**, 76–80 (2018).
4. Lucchini, M. et al. Attosecond dynamical Franz-Keldysh effect in polycrystalline diamond. *Science* **353**, 916–919 (2016).
5. Schultze, M. et al. Attosecond band-gap dynamics in silicon. *Science* **346**, 1348–1352 (2014).
6. Schiffrin, A. et al. Optical-field-induced current in dielectrics. *Nature* **493**, 70–74 (2013).
7. Schultze, M. et al. Controlling dielectrics with the electric field of light. *Nature* **493**, 75–78 (2013).
8. Silva, R., Jiménez-Galán, Á., Amorim, B., Smirnova, O. & Ivanov, M. Topological strong-field physics on sub-laser-cycle timescale. *Nat. Photon.* **13**, 849–854 (2019).
9. Jiménez-Galán, Á., Silva, R., Smirnova, O. & Ivanov, M. Lightwave control of topological properties in 2D materials for sub-cycle and non-resonant valley manipulation. *Nat. Photon.* **14**, 728–732 (2020).
10. Lakhotia, H. et al. Laser picoscopy of valence electrons in solids. *Nature* **583**, 55–59 (2020).
11. Cohen-Tannoudji, C. N. Nobel lecture: manipulating atoms with photons. *Rev. Mod. Phys.* **70**, 707 (1998).
12. Haroche, S. Nobel lecture: controlling photons in a box and exploring the quantum to classical boundary. *Rev. Mod. Phys.* **85**, 1083 (2013).
13. Sokolov, A. V., Walker, D. R., Yavuz, D. D., Yin, G. Y. & Harris, S. E. Raman generation by phased and antiphased molecular states. *Phys. Rev. Lett.* **85**, 562 (2000).
14. Jiangbin, G., Morales-Molina, L. & Hänggi, P. Many-body coherent destruction of tunneling. *Phys. Rev. Lett.* **103**, 133002 (2009).
15. Keldysh, L. et al. Ionization in the field of a strong electromagnetic wave. *Sov. Phys. JETP* **20**, 1307–1314 (1965).
16. Jürgens, P. et al. Origin of strong-field-induced low-order harmonic generation in amorphous quartz. *Nat. Phys.* **16**, 1035–1039 (2020).
17. Ghimire, S. et al. Observation of high-order harmonic generation in a bulk crystal. *Nat. Phys.* **7**, 138–141 (2011).
18. Vampa, G. et al. Theoretical analysis of high-harmonic generation in solids. *Phys. Rev. Lett.* **113**, 073901 (2014).
19. Hawkins, P. G. & Ivanov, M. Y. Role of subcycle transition dynamics in high-order-harmonic generation in periodic structures. *Phys. Rev. A* **87**, 063842 (2013).
20. You, Y. S. et al. Laser waveform control of extreme ultraviolet high harmonics from solids. *Opt. Lett.* **42**, 1816–1819 (2017).
21. Uzan, A. J. et al. Attosecond spectral singularities in solid-state high-harmonic generation. *Nat. Photon.* **14**, 183–187 (2020).
22. Dudovich, N. et al. Measuring and controlling the birth of attosecond XUV pulses. *Nat. Phys.* **2**, 781–786 (2006).
23. Pedatzur, O. et al. Attosecond tunnelling interferometry. *Nat. Phys.* **11**, 815–819 (2015).
24. Vampa, G. et al. Linking high harmonics from gases and solids. *Nature* **522**, 462–464 (2015).
25. Vampa, G. et al. All-optical reconstruction of crystal band structure. *Phys. Rev. Lett.* **115**, 193603 (2015).
26. Vampa, G. et al. Attosecond synchronization of extreme ultraviolet high harmonics from crystals. *J. Phys. B: At. Mol. Opt. Phys.* **53**, 144003 (2020).
27. You, Y. S., Reis, D. A. & Ghimire, S. Anisotropic high-harmonic generation in bulk crystals. *Nat. Phys.* **13**, 345–349 (2017).
28. Schubert, O. et al. Sub-cycle control of terahertz high-harmonic generation by dynamical Bloch oscillations. *Nat. Photon.* **8**, 119–123 (2014).
29. Wu, M. et al. Orientation dependence of temporal and spectral properties of high-order harmonics in solids. *Phys. Rev. A* **96**, 063412 (2017).

Methods

Dressed bands in strongly driven solids. We consider the response of a two-band solid driven by a strong low-frequency field, and we show how an effective band structure can be introduced in this case on the sub-cycle timescale, which is relevant for low-frequency drivers. In addition to a simple result that averages the instantaneous adiabatic energies over the current wavefunction, we introduce an extension of the Floquet-type analysis to the sub-cycle timescale.

Floquet-type analysis on the sub-cycle timescale: effective bandgap in a strong low-frequency field. Let us start with some well-defined eigenstate, with wavefunction $\psi_{\boldsymbol{\kappa}}$ and energies E_g, which satisfies the stationary Schrödinger equation, namely, $\hat{H}\psi_{\boldsymbol{\kappa}} = E_g\psi_{\boldsymbol{\kappa}}$. Here $\boldsymbol{\kappa}$ collects the quantum numbers that label the state. In a solid, $\boldsymbol{\kappa}$ labels the crystal momentum $\mathbf{k}$ together with band index n.

Let the Hamiltonian depend on some external parameter β, that is, $\hat{H}(\beta)$. If we change β slowly, our eigenstate will slowly evolve following the stationary Schrödinger equation

$$\hat{H}(\beta)\phi_{\boldsymbol{\kappa}}(\beta) = \epsilon_{\boldsymbol{\kappa}}(\beta)\phi_{\boldsymbol{\kappa}}(\beta). \tag{3}$$

In the low-frequency field, where the driver has frequency ω substantially lower than the energy gap, such parameter β is $\beta=\omega t$. From now on, we will simply refer to time t. In the low-frequency field, the adiabatic states are solutions of the stationary Schrödinger equation with time treated as a parameter:

$$\begin{aligned}\hat{H}(t)\phi_{\boldsymbol{\kappa}}(t) &= \epsilon_{\boldsymbol{\kappa}}(t)\phi_{\boldsymbol{\kappa}}(t),\\ \hat{H}(t) &= \hat{H}_0 + V(\hat{t}),\end{aligned} \tag{4}$$

where $V(t)$ is the interaction with the low-frequency field. The adiabatic eigenstates $\phi_{\boldsymbol{\kappa}}(t)$ form a complete basis set. Each state has an associated time-dependent state $\Psi_{\boldsymbol{\kappa}}$ that incorporates the standard energy phase factor as follows:

$$\Psi_{\boldsymbol{\kappa}}(t) = \mathrm{e}^{-\mathrm{i}\int_{t_i}^{t}\epsilon_{\boldsymbol{\kappa}}(t')\mathrm{d}t'}\phi_{\boldsymbol{\kappa}}(t). \tag{5}$$

Putting this back into the time-dependent Schrödinger equation, we see that the equation for $\Psi_{\boldsymbol{\kappa}}$ contains an extra term proportional to the derivative of the eigenstate:

$$\mathrm{i}\dot{\Psi}_{\boldsymbol{\kappa}} = H(\hat{t})\Psi_{\boldsymbol{\kappa}} + \mathrm{i}\mathrm{e}^{-\mathrm{i}\int_{t_i}^{t}\epsilon_{\boldsymbol{\kappa}}(t')\mathrm{d}t'}\dot{\phi}_{\boldsymbol{\kappa}}. \tag{6}$$

As long as the non-adiabatic Landau–Dykhne-type transitions (between the adiabatic states) caused by this term are small, their instantaneous energies $\epsilon_{\boldsymbol{\kappa}}(t)$ offer a very good approximation for the effective instantaneous (and hence the sub-cycle) energies of the driven system. However, in the presence of strong non-adiabatic transitions between the adiabatic states, these concepts require corrections.

Consider now the specific case of a solid, with bands $\epsilon_n(\mathbf{k})$ and Bloch wavefunctions $\phi_{n,\mathbf{k}}$, interacting with a low-frequency laser field. We note that the analysis below is not, in fact, limited to such a low-frequency case, but the low-frequency case presents the most natural physical situation where our analysis and its conclusions are physically transparent.

With the light–solid interaction treated in the dipole approximation and in the length gauge, the initial crystal momentum $\mathbf{k}$ becomes a function of time. We label this time-dependent momentum $\boldsymbol{\kappa}(t)=\mathbf{k}+\mathbf{A}(t)$, where $\mathbf{A}(t)$ is the field vector potential.

It is very useful then to use the Houston states to analyse the interaction. In this basis, Bloch wavefunctions $\phi_{n,\mathbf{k}}$ and band energies $\epsilon_n(\mathbf{k})$ also follow the vector potential, replacing $\mathbf{k}$ with $\boldsymbol{\kappa}(t)=\mathbf{k}+\mathbf{A}(t)$. The field-free energy $\epsilon_n(\mathbf{k})$ goes into $\epsilon_n(\boldsymbol{\kappa}(t))\equiv\epsilon_n(\mathbf{k}+\mathbf{A}(t))$, so that the band energy 'slides' with instantaneous momentum $\boldsymbol{\kappa}(t)$. The Bloch wavefunction also 'slides' with this instantaneous momentum, becoming $\phi_{n,\boldsymbol{\kappa}(t)}$.

In this basis, each time-dependent crystal momentum $\boldsymbol{\kappa}(t)=\mathbf{k}+\mathbf{A}(t)$ 'traces' its own multilevel system, with its states labelled with band index n as well as time-dependent energies and couplings. The multilevel system with crystal momentum $\mathbf{k}$ is decoupled from other multilevel systems with momenta $\mathbf{k}'$.

Beyond adiabatic evolution. Consider a two-band solid, with band indexes $n=1,2$, driven by a low-frequency field. Owing to the low frequency, the adiabatic evolution would be a good approximation for most part of the Brillouin zone. The adiabatic evolution will break down to the greatest extent in regions of the smallest bandgap, with exponential dependence on the bandgap.

Different $\mathbf{k}$ values reach these regions at different times and hence with different instantaneous values of field $\mathbf{F}(t)$. Suppose we start in state $\mathbf{k}$, turn on the field, and at a moment t_i, we arrive at some momentum $\boldsymbol{\kappa}$ in one of the adiabatic states (say with label $|1,\boldsymbol{\kappa}\rangle$), approaching a region where the two bands are coming close to each other.

We shall now look at the propagator across the region of interest. The analysis is general, but for the physical interpretation to be clear, the time interval should be enough to go through the region. For compactness, we will drop the crystal momentum index for the moment.

The propagator, written in the basis of the adiabatic states $|\Psi^{(1)}\rangle$ and $|\Psi^{(2)}\rangle$ with energies $\epsilon^{(1)}(t)$ and $\epsilon^{(2)}(t)$, respectively, has the following form:

$$\begin{aligned}\hat{U}(t,t_i) &= \mathrm{e}^{-\mathrm{i}\frac{1}{2}\left[\lambda^{(1)}+\lambda^{(2)}\right]}\begin{pmatrix}\cos\alpha\mathrm{e}^{\mathrm{i}\lambda} & -\sin\alpha\mathrm{e}^{\mathrm{i}\phi}\\ \sin\alpha\mathrm{e}^{-\mathrm{i}\phi} & \cos\alpha\mathrm{e}^{-\mathrm{i}\lambda}\end{pmatrix}.\\ \lambda &= \tfrac{1}{2}\left[\lambda^{(2)}-\lambda^{(1)}\right]\end{aligned} \tag{7}$$

This form of the propagator is general and meets the key requirements.

$$\begin{aligned}|U_{11}|^2+|U_{21}|^2 &= 1\\ |U_{12}|^2+|U_{22}|^2 &= 1\\ \hat{U}\hat{U}^\dagger &= \hat{U}^\dagger\hat{U} = \hat{\mathrm{I}}\end{aligned} \tag{8}$$

The last point also ensures that the wavefunctions remain orthogonal during passage, that is, $\langle\Psi^{(2)}|\hat{U}^\dagger\hat{U}|\Psi^{(1)}\rangle = 0$.

The meaning of the matrix elements in this propagator is as follows.

- The phases $\lambda^{(1,2)}(t)$ are associated with the adiabatic energies plus, in general, the geometrical Berry phase, γ_i.

$$\lambda^{(i)}(t) = \int_{t_i}^{t}\mathrm{d}t'\epsilon^{(i)}(t') + \gamma_i \tag{9}$$

  The reason we want to complete the passage across the region of interest is that we want the geometrical phase, associated with this passage, to accumulate fully. But, if we treat the problem fully numerically, then, of course, such a requirement is not necessary: the phases $\lambda^{(i)}(t)$ are simply found numerically.
- The overall factor in front of the propagator sets the zero-energy level as

$$\langle\epsilon\rangle = \frac{1}{2}\left[\epsilon^{(2)}+\epsilon^{(1)}\right] \tag{10}$$

  through the phases associated with the adiabatic energies.
- Irrespective of how the phases $\lambda^{(i)}(t)$ are obtained, their physical interpretation remains the same: their time derivatives have to be associated with the adiabatic energies (which are viable and meaningful in the absence of non-adiabatic transitions, that is, when $|\sin\alpha|\ll 1$).

$$\tilde{\epsilon}^{(i)}(t) = \frac{\partial\lambda^{(i)}(t)}{\partial t} \tag{11}$$

  The reason to add the 'tilde' above the adiabatic energy is to stress that the adiabatic energies $\tilde{\epsilon}^{(i)}(t)$ obtained in such a way may not always coincide with the adiabatic energies obtained by diagonalizing the adiabatic Hamiltonian, because of the presence of the geometric phase. Again, we stress that the phases associated with $\tilde{\epsilon}^{(i)}(t)$ can be numerically extracted. For the physical interpretation, we will need their derivatives.
- The off-diagonal elements describe the Landau–Zener–Dykhne non-adiabatic transitions between the two adiabatic states.
- Phases ϕ of these off-diagonal elements are determined by the landscape of the bands and the Berry connections (couplings). As we shall see below, the effective band structure is independent of ϕ.
- The probability of staying in the adiabatic state is $\cos^2\alpha$ and the probability of making the transition is $\sin^2\alpha$.

We can now develop the sub-cycle version of the Floquet analysis. To this end, we return to the propagator, dropping the common zero-energy-level phase factor for compactness, as

$$\begin{aligned}\hat{U}(t,t_i) &= \begin{pmatrix}\cos\alpha\mathrm{e}^{\mathrm{i}\lambda} & -\sin\alpha\mathrm{e}^{\mathrm{i}\phi}\\ \sin\alpha\mathrm{e}^{-\mathrm{i}\phi} & \cos\alpha\mathrm{e}^{-\mathrm{i}\lambda}\end{pmatrix}\\ \lambda &= \tfrac{1}{2}\left[\lambda^{(2)}-\lambda^{1)}\right]\end{aligned} \tag{12}$$

and look for orthogonal states $|\Psi^\mu(t_i)\rangle$ with time-dependent quasi-energies $\epsilon^\mu(t,t_i)$, which depend on crystal momentum $\mathbf{k}$. We want these states to behave as if they were the Floquet states for this propagator.

$$\begin{aligned}\hat{U}(t,t_i)\,|\Psi^\mu\rangle &= \mathrm{e}^{\mathrm{i}\mu}\,|\Psi^\mu\rangle\\ \epsilon^\mu &= -\tfrac{\partial\mu}{\partial t}\end{aligned} \tag{13}$$

The positive sign in the phase of the exponent is for convenience because we shall start with the 'lower' state, which has negative energy. The minus sign in the equation for the quasi-energy is related to the positive sign in the exponent in the first equation.

These quasi-energies and the associated states are as close as one can get to the effective bands and effective eigenstates in a strongly driven system with

non-adiabatic transitions. As we shall see below, in the absence of non-adiabatic transitions, they—of course—coincide with the adiabatic energies and states.

In principle, one can try to find such states for any time interval after t_i, but a meaningful time interval is an interval that is sufficient to cross the transition region. Once the region is crossed, each component of the wavefunction, projected on the adiabatic states, will mostly evolve on the associated adiabatic bands; in the absence of non-adiabatic transitions, these bands are fine and, as mentioned above, coincide with the quasi-energies discussed below.

The time-dependent 'eigenstates' of the propagator have two components corresponding to the amplitudes in the two adiabatic states $|\phi^{(i)}(t)\rangle$.

$$|\Psi^{\mu}\rangle = \begin{pmatrix} a_{\mu} \\ b_{\mu} \end{pmatrix} \tag{14}$$

The analysis is straightforward. We consider that the determinant of matrix $\hat{U} - e^{i\mu}\hat{1}$ is equal to zero, and the solution is found to be

$$\cos\mu = \cos\alpha\cos\lambda. \tag{15}$$

There are two solutions of this equation, namely, $\mu_1 = \mu$ and $\mu_2 = -\mu$, and the quasi-energies ϵ^{μ_1} and ϵ^{μ_2} are obtained by differentiating μ_1 and μ_2 with respect to time, respectively.

The first observation is that in the absence of non-adiabatic transitions, when $\cos\alpha = 1$, $\cos\mu = \cos\lambda$, $\mu_1 = -\lambda$ and $\mu_2 = \lambda$, and the quasi-energies coincide with the adiabatic states.

Equation (15) is already sufficient to find the effective bandgap, which is equal to

$$\Delta\epsilon^{\mu} = \left|\epsilon^{\mu_1} - \epsilon^{\mu_2}\right| = 2\left|\frac{\partial\mu}{\partial t}\right|. \tag{16}$$

We differentiate the two sides of equation (15) with respect to time and find

$$\Delta\epsilon^{\mu} = \left[\tilde{\epsilon}_{\mathrm{ad}}^{(2)} - \tilde{\epsilon}_{\mathrm{ad}}^{(1)}\right]\left|\cos\alpha\frac{\sin\lambda}{\sin\mu}\right|, \tag{17}$$

where we have used that

$$2\dot{\lambda} = \tilde{\epsilon}_{\mathrm{ad}}^{(2)} - \tilde{\epsilon}_{\mathrm{ad}}^{(1)}. \tag{18}$$

Using the relationship $\cos\mu = \cos\alpha\cos\lambda$, we can rewrite

$$\left[\cos\alpha\frac{\sin\lambda}{\sin\mu}\right]^2 = \frac{\cos^2\alpha\sin^2\lambda}{\cos^2\alpha\sin^2\lambda + \sin^2\alpha} \tag{19}$$

and hence

$$\Delta\epsilon^{\mu} = \left[\tilde{\epsilon}_{\mathrm{ad}}^{(2)} - \tilde{\epsilon}_{\mathrm{ad}}^{(1)}\right]\sqrt{\frac{\cos^2\alpha\sin^2\lambda}{\cos^2\alpha\sin^2\lambda + \sin^2\alpha}}. \tag{20}$$

Finally, we can simplify this expression by taking into account that if the action $\lambda(t)$ is large, which is usually the case in a strong, low-frequency field, then $\sin^2\lambda(t, t_i)$ is a fast-oscillating function of $t - t_i$. Replacing it with its average ($\sin^2\lambda(t, t_i) \Rightarrow 1/2$) and introducing the notation $\sin^2\alpha = w_{\mathrm{LD}}$, we get the final result for the bandgap between the two quasi-energies as

$$\Delta\epsilon^{\mu} = \left[\tilde{\epsilon}_{\mathrm{ad}}^{(2)} - \tilde{\epsilon}_{\mathrm{ad}}^{(1)}\right]\sqrt{\frac{1 - w_{\mathrm{LD}}}{1 + w_{\mathrm{LD}}}}. \tag{21}$$

This result shows that the bandgap collapses when the non-adiabatic Landau–Dykhne-type transition approaches unity, that is, $w_{\mathrm{LD}} \simeq 1$.

We note that the formalism based on the sub-cycle analogue of the quasi-energy states of a strongly driven system is especially attractive because it naturally merges into the Floquet analysis when $t - t_i$ is equal to one period.

One can also find the quasi-eigenenergies in a different way by only using the relationship $\cos\mu = \cos\alpha\cos\lambda$. Namely, one can use this relationship to solve the equations for the amplitudes a^{μ} and b^{μ}, and then average the full Hamiltonian over the eigenvectors obtained in such a way from equation (14). The result is exactly the same, as expected.

Data availability

The data and datasets that support the plots within this paper and other findings of this study are available from the corresponding author upon reasonable request.

Code availability

The custom code used for the current study has been described in previous publications, and parts of it can be made available from the corresponding author on reasonable request.

Acknowledgements

N.D. is the incumbent Robin Chemers Neustein Professorial Chair. N.D. acknowledges the Minerva Foundation, the Israeli Science Foundation and the European Research Council for financial support. A.J.U.-N. acknowledges financial support by the Rothschild Foundation and the Zuckerman Foundation. M.I. acknowledges funding from the DFG QUTIF grant IV152/6-2. Á.J.-G. acknowledges funding from the European Union's Horizon 2020 research and innovation programme under the Marie Skłodowska-Curie grant agreement no. 101028938. Á.J.-G. and M.I. acknowledge funding from the European Union's Horizon 2020 research and innovation programme under grant agreement no. 899794. R.E.F.S. acknowledges support from the fellowship LCF/BQ/PR21/11840008 from 'La Caixa' Foundation (ID 100010434) and from the European Union's Horizon 2020 research and innovation programme under the Marie Skłodowska-Curie grant agreement no. 847648.

Author contributions

N.D. and M.I. supervised the study. M.I. supervised the theoretical work and developed the theoretical model. A.J.U.-N. and G.O. conceived and planned the experiments. Á.J.-G. and R.S. performed the theoretical study and numerical analysis. A.J.U.-N., T.A.-P., G.O. and B.D.B performed the measurements. A.J.U.-N., G.O. and S.S. analysed the data. B.Y. performed the DFT calculations. All the authors discussed the results and contributed to writing the manuscript.

Competing interests

The authors declare no competing interests.

Additional information

Supplementary information The online version contains supplementary material available at https://doi.org/10.1038/s41566-022-01010-1.

Correspondence and requests for materials should be addressed to Nirit Dudovich.

Peer review information *Nature Photonics* thanks Dieter Bauer and the other, anonymous, reviewer(s) for their contribution to the peer review of this work.